Supporting Information

A factor two improvement in high-field dynamic nuclear polarization from Gd(III) complexes by design.

Gabriele Stevanato[a], Dominik Józef Kubicki[a], Georges Menzildjian[a], Anne-Sophie Chauvin[b], Katharina Keller[c], Maxim Yulikov[c], Gunnar Jeschke[c], Marinella Mazzanti[b] and Lyndon Emsley*[a]

[a.] *Institut des Sciences et Ingénierie Chimiques, Ecole Polytechnique Fédérale de Lausanne (EPFL), CH-1015 Lausanne, Switzerland.*
[b.] *Group of Coordination Chemistry, Institut des Sciences et Ingénierie Chimiques, Ecole Polytechnique Fédérale de Lausanne (EPFL), CH-1015 Lausanne, Switzerland*
[c.] *ETH Zurich, Department of Chemistry, Laboratory of Inorganic Chemistry, 8093 Zurich, Switzerland.*

1 Table of Contents

2 MAS-DNP NMR Methods

2.1 Experimental setup:

DNP-enhanced NMR experiments were performed on a commercial Bruker 400 MHz spectrometer, with a Bruker Avance III console and a triple resonance 3.2 mm low temperature DNP CP-MAS probe. A gyrotron providing high-power microwave irradiation at 263 GHz at the sample position via a corrugated wave-guide was used. The gyrotron operates continuously during the MAS-DNP experiment with a cavity temperature of 22.5 ± 0.2 °C and at an optimized collector current. The stability of the microwave power is estimated around ± 1%.

3.2 mm sapphire rotors were used to ensure optimal microwave penetration. The solution under study was confined within the rotor by the addition of a silicone plug and with a ZrO_2 cap.

The experiments were performed at a spinning frequency of either at 8 kHz ± 5 Hz or at 10 kHz ± 5 Hz controlled by a MAS II cryo-cabinet, in order to reduce the overlap between the compound and the silicone resonances.

2.2 Field-sweep unit:

The field sweep measurements to record the Zeeman field profiles used a Lakeshore unit (Model 625) which provided an extra current to change the main magnetic field. When setting the current value an overshoot of 10% was used for steps <5.5 A, whereas 0.55 A for steps >5 A. The overshoot occurs in the same direction as current step. The overshoot is meant to minimize the main magnetic field drift.

2.3 Probe configuration:

The experiments for the estimation of the ^{1}H, ^{13}C, ^{15}N Zeeman field profiles used a Bruker DNP CP-MAS probe in $\lambda/4$-triple mode with a ^{13}C-insert (15 pF // 9 t) without a serial capacitor and with a 22 pF shunt capacitor to reach the 40 MHz ^{15}N frequency on the Y channel.

2.4 Pulse sequences and experimental parameters:

^{13}C and ^{15}N 1D direct excitation experiments were performed with a rotor synchronized spin echo pulse sequence with/without microwave excitation. The pulse sequence is: saturation-d1-$\pi/2$-τ-π-τ-acquisition. The delays τ were set to one rotor period. The saturation train always precedes the delay d1 before the $\pi/2$ pulse to destroy any residual magnetization.

^{1}H-T_1 and polarization build-up times T^{DNP} were measured with a saturation recovery pulse sequence with echo detection: saturation-$\tau_{recovery}$-$\pi/2$-τ-π-τ-acquisition.

The ^{1}H DNP enhancement was estimated via ^{1}H-^{13}C CP experiments (see **Figure SI-1a**). The recycle delay was varied between 10s and 60s depending on the sample concentration and polarization build-up time. For the direct ^{13}C and ^{15}N enhancement the delay was of 30 s for ^{13}C and 40 s for ^{15}N experiments. Experimental parameters are gathered in **Table SI-1**.

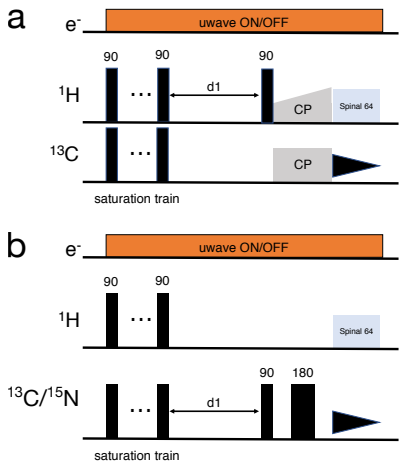

Figure SI-1: (a) Pulse sequence used for ^{1}H-^{13}C CP experiments. The delay d_1 is set as 1.3 T^{DNP}. T^{DNP} indicates the build-up time of ^{1}H polarization. (b) Pulse sequence used for direct ^{13}C and ^{15}N experiments. The initial saturation pulse train is used to destroy any residual magnetization before signal acquisition.

^{1}H 1D echo-detected	
π/2 and π pulses	3µs and 6µs
Acquisition time (s)	0.0273067
TD	16384
D1 (s)	3
^{1}H-^{13}C CP	
^{1}H π/2 pulse	5µs
Contact time	2 ms / 500 µs (^{13}C-2, ^{15}N glycine sample)
Linear ramp	90/100
CP power level ^{13}C	83.3 kHz
CP power level ^{1}H	48.7 kHz
^{1}H decoupling (SPINAL 64)	Not used
Acquisition time (s)	0.0245760
TD	4096
Line broadening	50 Hz
D1 (s)	16
^{13}C direct	
^{13}C π/2 pulse	3 µs
power level ^{13}C	134.4 W (83.3 kHz)
^{1}H decoupling (SPINAL 64)	77 kHz
Acquisition time (s)	0.04096
TD	16384
Line broadening	150 Hz
D1	30 s
^{15}N direct	
^{15}N π/2 pulse	5.5 µs
power level ^{15}N	180 W (45.4 kHz)
^{1}H decoupling (SPINAL 64)	77 kHz
Acquisition time (s)	0.0122880
TD	2048
Line broadening	150 Hz
D1	40 s

Table SI-1: Typical set of experimental parameters used for the different MAS-DNP experiments at 400 MHz.

2.5 Sample preparation:

The sample for the experiment collecting the direct ^{13}C and ^{15}N [Gd(dota)(H_2O)]$^{-}$ field profiles reported in **Figure SI-4** was a solution of 20 mM [Gd(dota)(H_2O)]$^{-}$ and 1.5M ^{13}C-2,^{15}N glycine in DNP juice, i.e. glycerol-d_8:D_2O:H_2O (6:3:1 v%). The mixture was sonicated in a warm (65°C) bath for 30 minutes until a transparent solution was obtained. Sonication was only used in the case of the samples containing glycine to help solubilization.
The experiments reported in **Figure 4** in the main text used a 5 mM solution of complex with 1.5 M ^{13}C,^{15}N enriched urea in DNP juice. The samples for the concentration dependence study reported in **Figure 5** of the main text were prepared by stirring the solid complex powders at 1000 rpm in DNP juice for 90 minutes in a warm bath at 45°C, as well as the samples used for the experiments with ascorbic acid presented in **Figure 1** of the main text and **Figure SI-5**.

Note that the stability of [Ln(tpatcn)] complexes was previously investigated in aqueous media at room temperature, and the complex remains undissociated in water in the pH range 3-8.[1] Moreover, earlier proton NMR studies on [Ln(tpatcn)] complexes[2] confirm the absence of exchange even at elevated temperature (343 K). These data exclude the possibility of any ligand exchange at the pH of the DNP juice (pH > 4). Moreover, exchange of the nonadentate trianionic tpatcn ligand with neutral monodentate ligands such as glycine and urea cannot be envisaged.

2.6 MAS-DNP enhancement:

The enhancement is calculated as the ratio between microwave ON/OFF signals at 100 K and under 8 kHz MAS in **Figure 1, 4** and **5** in the main text, as well as other figures in the SI, and 10 kHz MAS in **Figure SI-5**. The uncertainty in $\varepsilon_{C\ CP}$ was assumed to be 10% for all measurements.

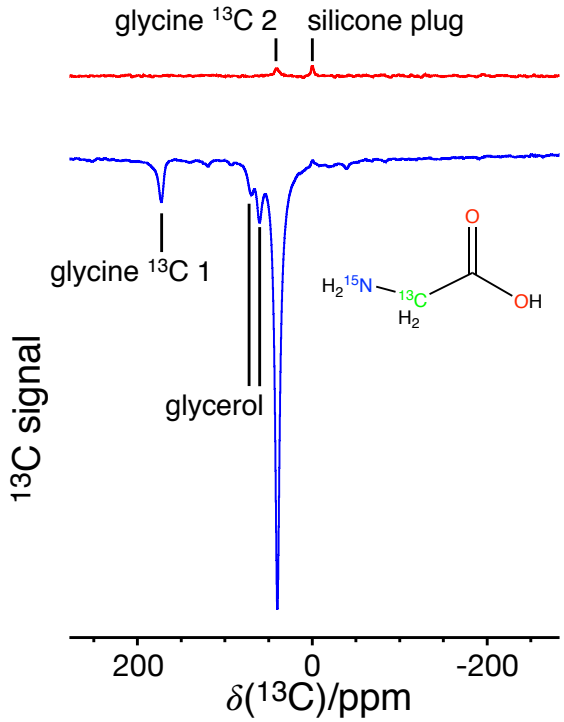

Figure SI-2: ^{13}C spectrum via direct ^{13}C acquisition (as per sequence in **Figure SI-1b**) with and without microwave irradiation in blue and red respectively for the solution used in the experiment described in **Figure SI-4**. The enhancement is estimated via the intensity of the glycine ^{13}C 2 peak. 16 scans were collected in both experiments.

3 MAS-DNP NMR results

3.1 MAS-DNP enhancement in the presence of dielectric crystal particles

In order to improve the microwave penetration and homogeneity in the sample, dielectric crystal particles (here, manually ground sapphire particles) were added to the sample, following the preparation protocol described in **[1]**. This sample formulation yields more than a 2-fold increase for the proton enhancement, from the same 10 mM [Gd(tpatcn)] solution without sapphire particles (see Figure 5 in the main text).

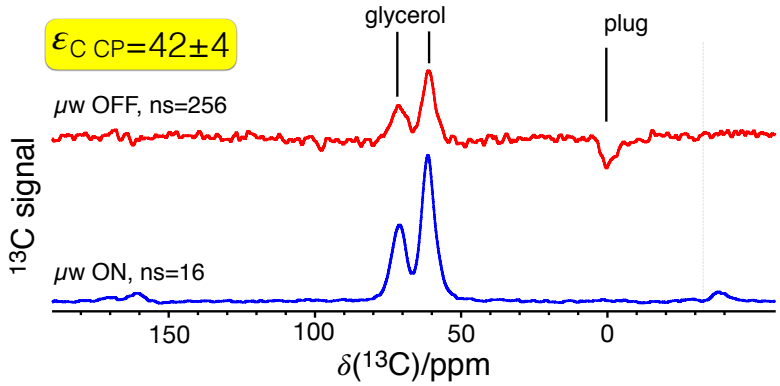

Figure SI-3: ^{13}C CP spectrum for 10 mM solution of **(1)** in glycerol-d_8:D_2O:H_2O (6:3:1 v%) at 100 K in presence of manually ground sapphire particles. The 3.2 mm rotor contains 12 µL of 10 mM solution (1/3 of the usual volume) and the remaining volume is filled with manually ground sapphire particles that have a relative permittivity of ϵ_R=9.6 [3]. The enhancement is $\varepsilon_{C\ CP}$~42±4, a factor of more than two times better than the enhancement without dielectric particles (see **Figure 5** in the main text).

3.2 Direct ^{13}C and ^{15}N enhancements and Zeeman field profiles

We prepared a solution containing 20 mM of [Gd(dota)(H_2O)]$^-$ and 1.5 M of glycine-2-^{13}C,^{15}N in glycerol-d_8:D_2O:H_2O (6:3:1 v/v/v %). The labelled ^{13}C and ^{15}N sites facilitate the direct estimation of ^{13}C and ^{15}N DNP enhancements. By sweeping the external magnetic field between 9.40 T and 9.47 T the ^{1}H enhancement via ^{13}C CP and the direct ^{13}C, on the glycine-2-^{13}C peak, and ^{15}N enhancements, on the glycine-^{15}N peak, were measured (see **Figure SI-2** and **Figure SI-4**).

At 20 mM of [Gd(dota)(H_2O)]$^-$ the maximum enhancements are: -15±2 for ^{1}H, 77±8 for ^{13}C, and 95±10 for ^{15}N. The positive lobe on the ^{13}C CP field profile for ^{1}H enhancement estimation at ~9.47 T has a smaller intensity than the negative lobe (see **Figure SI-4**). This is most likely due to the consistent field drift observed in that region of magnetic field which spreads the peak over a wider range of frequencies during the NMR experiment. We also report an interesting occurrence in the direct ^{13}C and ^{15}N spectra, previously observed for ^{13}C in labelled urea in ref. [4]. A small ^{13}C and ^{15}N enhancement is present at the field positions corresponding to the ^{1}H SE DNP lobes. It is of inverse sign in the case of ^{13}C (with γ(^{13}C)>0) whereas of the same sign for ^{15}N (with γ(^{15}N)<0) with respect to ^{1}H (see **Figure SI-4**). This effect has been attributed to heteronuclear cross relaxation processes. The ^{1}H population far from thermal equilibrium under DNP conditions at ~9.44T and ~9.47T might enhance the ^{13}C and ^{15}N signals through the classical nuclear Overhauser effect.

The distance between negative and positive peaks in the ^{1}H and ^{13}C field profiles is consistent with a *solid effect* mechanism, as the equation ω_{0S+}-ω_{0S-} ~$2\omega_{0I}$ is satisfied. For ^{15}N ω_{0S+}-ω_{0S-} ~55 MHz~1.37ω_{0I}. In this case a contribution of both *solid effect* and *cross effect* mechanisms is possible. This does not come as a surprise considering that the [Gd(dota)(H_2O)]$^-$ linewidth is <22 MHz, whereas the ^{15}N Larmor frequency at 9.4 T is ~40 MHz.

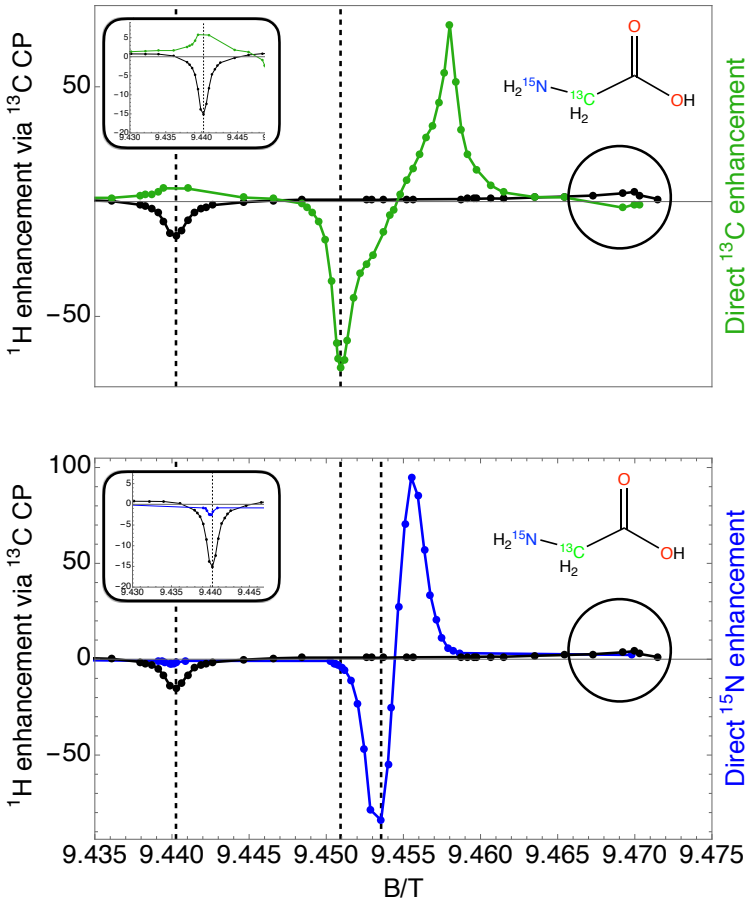

Figure SI-4: DNP Zeeman field profiles at 100 K of a 20 mM solution of [Gd(dota)(H_2O)]$^-$ and 1.5 M glycine-2-^{13}C,^{15}N in glycerol-d_8:D_2O:H_2O (6:3:1 v%). Each point in panel a) is the intensity of the glycine-2-^{13}C signal recorded via ^{13}C CP (black points) or direct ^{13}C acquisition (green points) and return the ^{1}H and ^{13}C field profiles respectively. In panel b) the direct ^{15}N (blue points) and the ^{1}H (black points) profiles are superimposed. The vertical dashed lines indicate the magnetic fields for the ^{1}H, ^{13}C and ^{15}N negative DNP. The black solid circles indicate magnetic field regions where the direct ^{13}C and ^{15}N field profiles exhibits extra features attributed to heteronuclear ^{1}H-X cross relaxation.

3.3 Polarization build-up times

The polarization build-up curves acquired in presence of microwave irradiation for **(1)** and **(2)**, and returning the polarization build-up time, have been fitted using a stretched exponential function $I(t)=I_0(1-Exp(-(t/Tb)^{\beta}))$.
Every point represents the integral of the glycerol peaks at different delay times after saturation. The values of Tb and β for the data at different concentrations presented in **Figure 5** of the main text are reported together with experimental points and fits in **Table SI-2**.

mM	Gd(tpatcn)	Gd(dota)
1	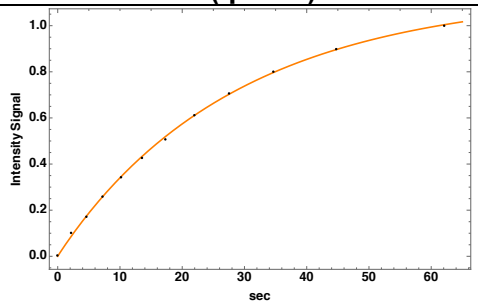 Tb=27.9±1.4 s β=0.95±0.02	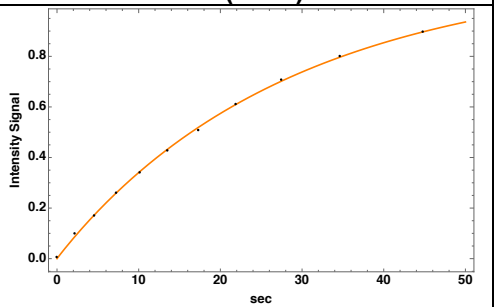 Tb=28.7±1.2 s β=0.98±0.02

2	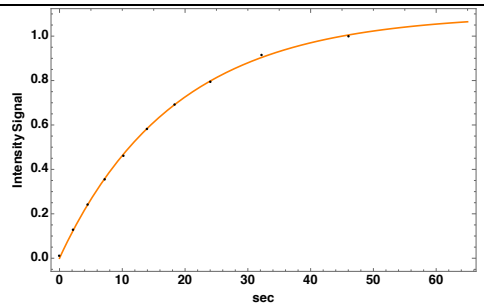 Tb=17.8±0.4 s β=1.02±0.02	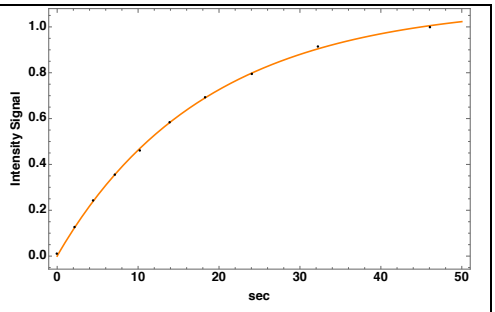 Tb=18.5±0.7 s β=0.98±0.02
3	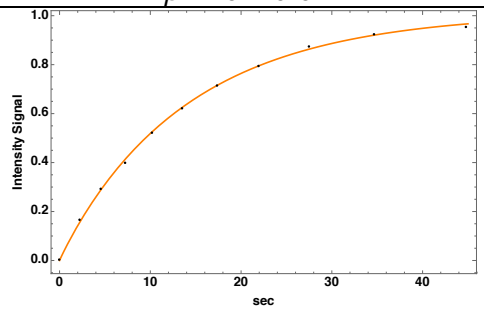 Tb=13.3±0.4 s β=1.04±0.02	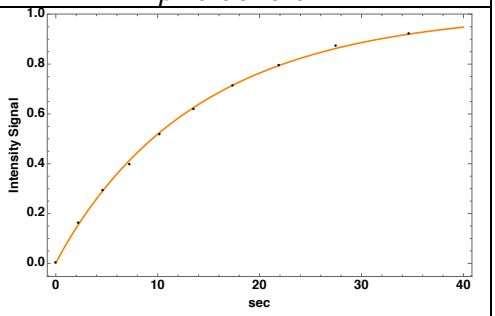 Tb=14.1±0.3 s β=0.96±0.02
4	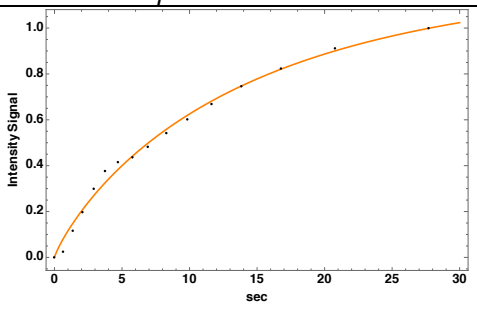 Tb=14.5±3.2 s β=0.85±0.06	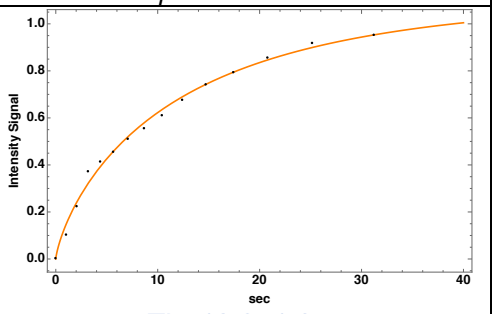 Tb=12.8±1.6 s β=0.76±0.05
5	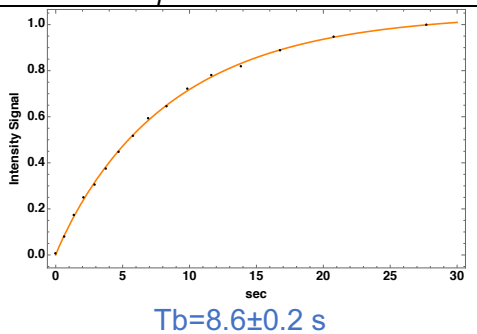 Tb=8.6±0.2 s β=0.95±0.02	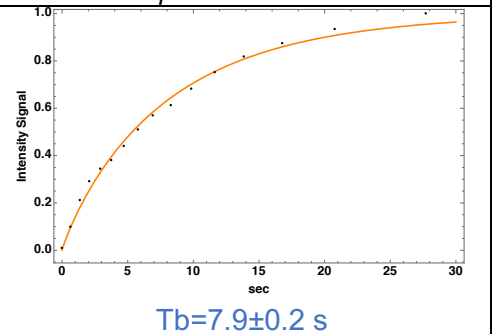 Tb=7.9±0.2 s β=0.90±0.03
6	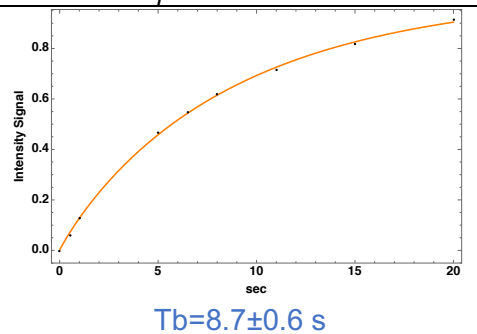 Tb=8.7±0.6 s β=0.93±0.03	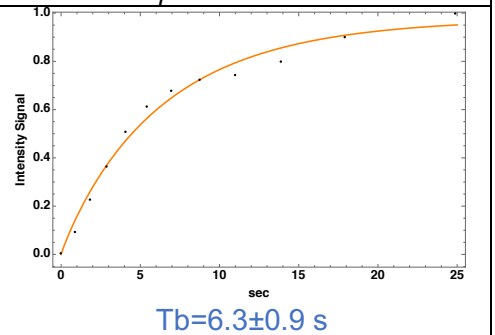 Tb=6.3±0.9 s β=0.94±0.10

8	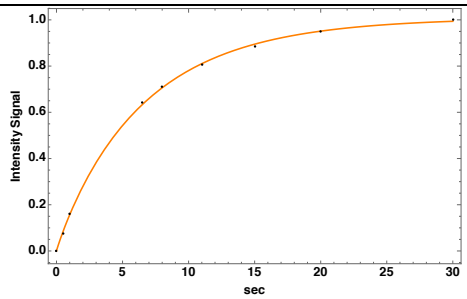 Tb=6.6±0.2 s β=0.94±0.02	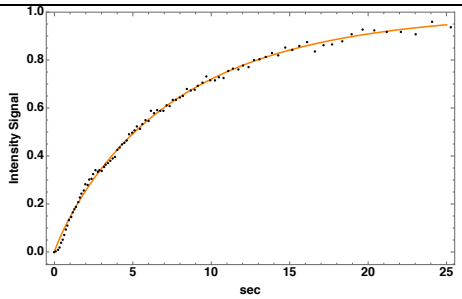 Tb=7.6±0.12 s β=0.90±0.01
10	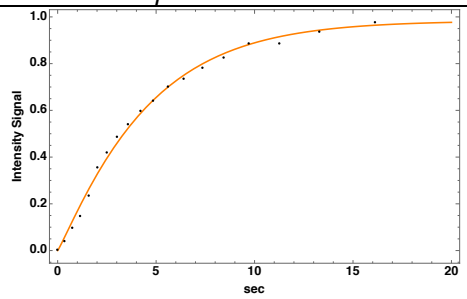 Tb=4.6±0.2 s β=1.09±0.04	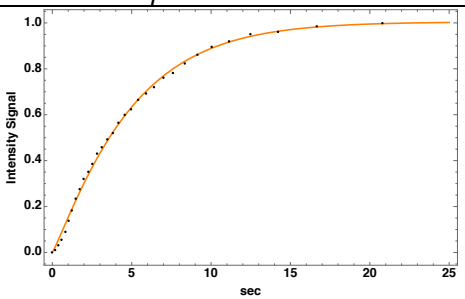 Tb=5.0±0.1 s β=1.12±0.02
12	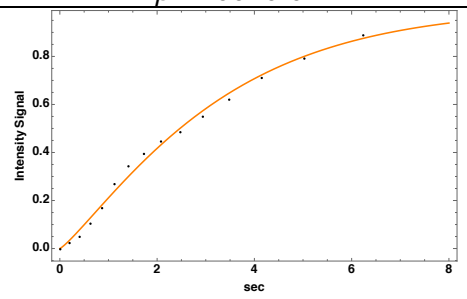 Tb=3.3±0.1 s β=1.2±0.05	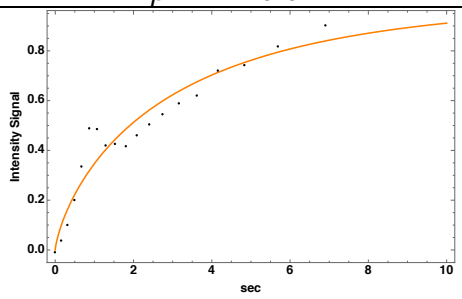 Tb=3.1±0.2 s β=0.75±0.08

Table SI-2: Fits of the polarization build-up curves (every point represents the integral of the glycerol peaks at different delay times after saturation) for Gd(tpatcn) and Gd(dota) across the explored concentration range (1-12 mM). The extracted polarization build-up times are reported, as well as the stretched exponential parameters used for the fits.

3.4 Enhancement vs PA concentration

The enhancements, but not their ratios, in Figure 5 are about 30% lower than those observed in Figure 4 for both **(1)** and **(2)**. We attribute this to the presumably higher sample temperature for the spectra of Figure 5 (due to reduced cooling N_2 gas flow capacity of 28 L/min vs the ideal 35 L/min) and to possibly non-optimal microwave irradiation (due to ice formation over time in the probe waveguide).

3.5 Enhancement vs ^{1}H concentration

We have also tested two different ^{1}H concentration by varying the H_2O content in the solvent formulation. The first sample was 4 mM Gd(tpatcn) in glycerol-d_8:D_2O:H_2O (6:3:1 v%) corresponding to a [^{1}H]~11M. The second was 4 mM Gd(tpatcn) in glycerol-d_8:H_2O (5:5 v%) corresponding to a [^{1}H]~55M. The results are summarized in the table below.

[^{1}H] / M	$\varepsilon_{C\ CP}$	Tb/s
11	35.5±3.5	14.5±3.2
55	17.9±1.8	10.0±1.0

Table SI-3: Enhancement factors ($\varepsilon_{C\ CP}$) and polarization build-up times (Tb/s) for 4 mM Gd(tpatcn) in glycerol-d_8:D_2O:H_2O (6:3:1 v%) (11 M ^{1}H concentration) and glycerol-d_8:H_2O (5:5 v%) (55 M ^{1}H concentration).

3.6 MAS-DNP of ascorbic acid

Here below we show the MAS-DNP and EPR results obtained for two solutions of 8 mM **(1)** + 1.3 M ascorbic acid and 10 mM AMUPol + 1.3 M ascorbic acid in glycerol-d_8:D_2O:H_2O (6:3:1 v%). The X-band EPR measurements are performed at room temperature, whereas MAS-DNP experiments are performed at 9.4 T and around 100 K. As expected, only **(1)** can be used as suitable PA for ascorbic acid, yielding ^{1}H enhancement of 24 at 9.4 T and 100 K.
No signal enhancement is observed when AMUPol is used as the polarization source, since it is immediately reduced to a diamagnetic form, and EPR (Figure SI 5d) confirms that there is no free radical present in the solution.

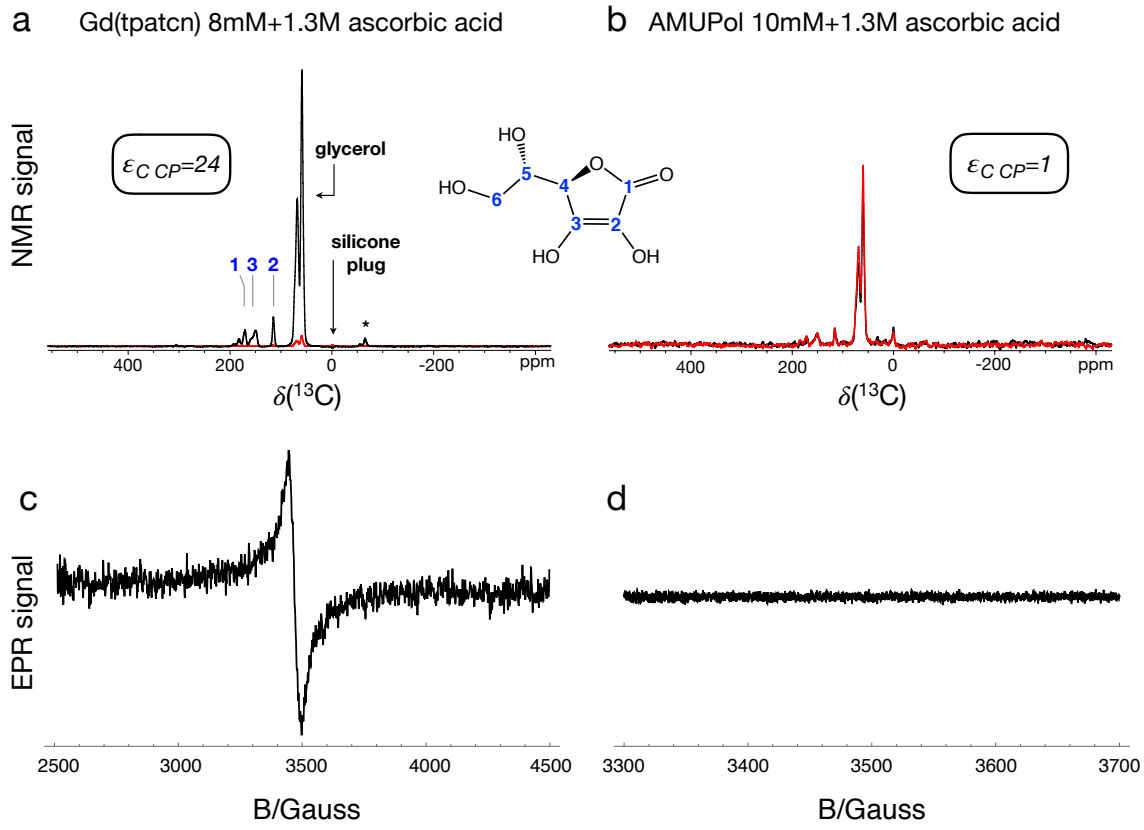

Figure SI-5: MAS-DNP $\varepsilon_{C\ CP}$ ^{1}H enhancements for 1.3 M ascorbic acid in glycerol-d_8:D_2O:H_2O (6:3:1 v%) in (a) using 8 mM complex **(1)**, whereas in (b) using 10 mM AMUPol. The microwave ON/OFF signals are in black/red respectively. The room temperature X-band EPR spectra for ascorbic acid + 8 mM complex **(1)** and ascorbic acid + 10 mM AMUPol in glycerol-d_8:D_2O:H_2O (6:3:1 v%) are represented in (c) and (d) respectively. The subpanels (b) and (d) illustrate the quenching of the nitroxide radicals, and thus the impossibility to use AMUPol as PA, due to the reducing nature of ascorbic acid.[5]

4 Theoretical appendix

In DNP theory, the solid effect mechanism can be modelled as a two-spin process involving one electron spin and one nuclear spin.[6] In the case of a radical with electron spin S=1/2 and a nuclear spin I=1/2, it can be shown that the evolution of the nuclear spin polarisation (P_I) upon microwave irradiation has the following form:[7]

$$\frac{\partial P_I}{\partial t} = -W_h^+(P_I - P_S) - W_h^-(P_I + P_S) \quad \text{(S 1)}$$

where P_S is the electron spin polarization and $W^{\pm}_h$ are transition rates defined by the following equation:

$$W_h^{\pm} = \frac{1}{2}\pi \frac{\left|\frac{1}{2}A_{z+}\right|^2 \omega_{1S}^2}{\omega_{0I}^2} h(\omega_S - \omega_m \mp \omega_{0I}) \quad \text{(S 2)}$$

where A_{z+} is the super-hyperfine interaction constant, ω_S and ω_{0I} are the electron and nuclear Larmor frequencies, ω_{1S} and ω_m the amplitude and frequency of the microwave field. The function $h(\omega)$ defines the homogeneous part of the electron linewidth. Substitution into equation (S 1) returns the usual DNP profile (similar to those measured experimentally and presented in **Figure SI-4**) with a negative and a positive local maximum separated in frequency by $2\omega_{0I}$:[7]

$$\frac{\partial P_I}{\partial t} = \frac{1}{2}\pi \frac{\left|\frac{1}{2}A_{z+}\right|^2 \omega_{1S}^2}{\omega_{0I}^2} [h(\omega_S - \omega_m - \omega_{0I}) - h(\omega_S - \omega_m + \omega_{0I})] P_S \quad \text{(S 3)}$$

In the case of high-spin electron systems (S>1/2), the analysis is further complicated by the presence of multiple energy levels that might be involved in the DNP mechanism and by the presence of anisotropic broadening mechanisms. For our purposes, following the experiments presented in **Figure SI-4** and **Figure 3** and **4** in the main text, we can qualitatively assume that the Gd(III) EPR linewidth is determined by the central transition (m_s=-1/2<->m_s=+1/2), which is broadened by second order mechanisms proportional to D^2/ω_S with D being the ZFS axial parameter. Any other contribution to line broadening is disregarded. In this way, we can formally treat a S>1/2 system like a pseudo S=1/2. We model the electron linewidth with a Lorentzian profile (but the same result would be obtained in the case of a different analytical lineshape):

$$h(\omega_S \pm \omega_{0I} - \omega_m) = \frac{\Delta_h}{\pi(\Delta_h^2 + (\omega_S \pm \omega_{0I} - \omega_m)^2)} \quad \text{(S 4)}$$

centred at $\omega_S \pm \omega_{0I}$ with a FWHM (Full Width Half Maximum)=Δ_h (see **Plot S-1**). By substituting (S 4) in (S 3), and using the parameters reported in the caption we obtain the profile in **Plot S-1**.

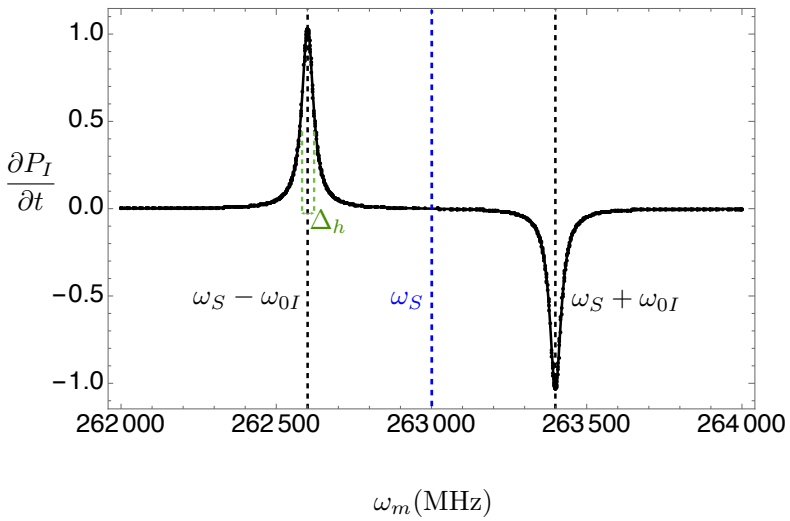

Plot S-1: Plot of equation (S 3) using a Lorentzian lineshape model for h(ω) (S 4) with the following parameters: $\Delta_h = 22\ MHz$, $\omega_S = 263000\ MHz$, $\omega_{0I} = 399\ MHz$, $\omega_{1S} = 0.52\ MHz$, $A_{z+} = 10\ MHz$. P_S has been arbitrarily chosen in order to normalize dP_I/dt. The dashed lines correspond to the positive and negative lobes of the microwave frequency profile. Their separation, for the solid effect DNP, is expected to be twice the nuclear Larmor frequency.

If we irradiate at $\omega_m = \omega_S - \omega_{0I}$, we obtain an evolution given by:

$$\frac{\partial P_I}{\partial t} = \frac{1}{2}\pi \frac{\left|\frac{1}{2}A_{z+}\right|^2 \omega_{1S}^2}{\omega_{0I}^2} \times \frac{\Delta_h}{\pi(\Delta_h^2 + (\omega_S - \omega_{0I} - \omega_m)^2)} P_S = \frac{1}{2}\pi \frac{\left|\frac{1}{2}A_{z+}\right|^2 \omega_{1S}^2}{\omega_{0I}^2} \times \frac{\Delta_h}{\pi(\Delta_h^2)} P_S = \frac{1}{2} \frac{\left|\frac{1}{2}A_{z+}\right|^2 \omega_{1S}^2}{\omega_{0I}^2} \times \frac{1}{\Delta_h} P_S \quad \text{(S 5)}$$

Equation (S 5) returns the time evolution of the nuclear spin polarization as a function of A_{Z+}, ω_{1S}, ω_{0I}, P_S and Δ_h.
For high-spin systems, the ZFS interaction can be expressed by the Hamiltonian:

$$H^{ZFS} = D\left(S_z^2 - \frac{1}{3}S(S+1)\right) + E(S_x^2 - S_y^2) \quad \text{(S 6)}$$

Where *D* and *E* represent the axial component and rhombicity of the electron-electron dipole interaction. If Δ_h is dominated by the ZFS interaction:

$$\Delta_h = \frac{D^2}{\omega_S} \quad \text{(S 7)}$$

Finally, if we consider two species (e.g. **(1)** and **(2)**), and if we assume that the other parameters are the same in both species, then the ratio of the nuclear polarization within the approximations used here is predicted to be:

$$\frac{\partial P_{(1)}}{\partial P_{(2)}} \propto \frac{\Delta_{h(2)}}{\Delta_{h(1)}} \propto \frac{D_{(2)}^2}{D_{(1)}^2} = \left(\frac{D_{(2)}}{D_{(1)}}\right)^2 \quad \text{(S 8)}$$

With $D_{(i)}$ being axial component of the ZFS of species **(i)**. The ratio $\partial P_{(1)}/\partial P_{(2)}$ in (S 8) should be the same as the ratio of the maximum signal intensities that we have determined experimentally (**Figure 4** in the main text).

Here, $\left(\frac{D_{(2)}}{D_{(1)}}\right)^2 = 1.95$ for **(1)** and **(2)**, which is very close to the factor of 2 (1.9 on average in **Figure 5**) determined experimentally (**Figure 5** in the main text).

We can also apply equation (S 8) to compare the ratios of ZFS parameters for a different *S*>1/2 system. In reference [8],[1]H enhancements of 12.8 and 3.5 respectively are reported for $[Gd(dota)(H_2O)]^-$ and $[Gd(dtpa)(H_2O)]^{2-}$. It is also assumed that D_{dtpa}=1440 MHz. Using the measured value ($D_{(2)}$=733 MHz) for $[Gd(dota)(H_2O)]^-$, we would predict an enhancement for $[Gd(dtpa)(H_2O)]^{2-}$: $12.8\times(733/1440)^2$ ~3.3, which is in good agreement with the reported enhancement of 3.5 [8].

This simple model does not consider MAS, does not include extra contributions to line broadening, which may in particular dominate at higher concentrations and does not account for the distribution of ZFS in a frozen solution at 100 K (see EPR analysis part below). Within this simplified framework, *the analysis predicts a quadratic dependence between the reduction by a factor r in ZFS and a gain in DNP enhancement proportional to r^2. The analysis is in excellent agreement with the experimental results so far.*

5 Synthesis

Gadolinium(III) 1,4,7,10-Tetraazacyclododecane-1,4,7,10-tetraacetate (indicated as $[Gd(dota)(H_2O)]^-$) was purchased from Macrocyclics and used without further purification. Theoretical formula: $GdC_{16}H_{24}N_4O_8Na.4H_2O$. [Gd(tpatcn)] was synthesised as reported in [2].

6 EPR experiments

6.1 EPR Methods

A 20 mM stock solution of [Gd(tpatcn)] and a 50 mM stock solution of $[Gd(dota)(H_2O)]^-$ were diluted to final concentrations of 25 µM and 10 mM in glycerol-d_8:D_2O:H_2O 6:3:1 %v. The sample solutions were filled into 0.5 mm i.d./0.9 mm o.d. quartz capillaries for W band and 3 mm o.d. quartz capillaries for X- and Q-band measurements. The samples were subsequently shock-frozen by immersion into liquid nitrogen before insertion into the microwave resonator at low temperature.
EPR experiments were performed on a commercial Bruker Elexsys E680 X-/W-Band spectrometer and a home-built high-power Q-band pulse EPR spectrometer[9] equipped with a rectangular cavity accommodating oversized 3 mm outer diameter cylindrical samples.[10-11]. For W-band measurements, the spectrometer was equipped with a Bruker TE011 resonator operating at roughly 94 GHz. For X-band measurements, the spectrometer was equipped with a Bruker MS3 split-ring resonator operating at frequencies of approximately 9.3 GHz. A helium flow cryostat (ER 4118 CF, Oxford Instruments) was used to adjust the measurement temperature to 10 or 100 K.

Echo-detected (ED) field-swept EPR spectra were acquired using a Hahn-echo pulse sequence $t_p - \tau - 2t_p - \tau$ – echo with a pulse length t_p of 12 ns. The interpulse delay τ was set to 400 ns at 10 K and 100, 200 or 400 ns at 100 K. The power to obtain the π/2 – π pulses was set at the central transition of the Gd(III) spectrum by nutation experiments. The same sequence was used to measure Hahn echo decay curves at 100 K, in which the delay τ was incremented (τ_0 = 100 or 200 ns). Longitudinal relaxation measurements were performed using an inversion recovery sequence $t_{inv} - T - t_{p,sel} - \tau - 2t_{p,se} - \tau$ – echo with an inversion pulse π pulse of t_{inv} = 16 ns and selective detection pulses with $t_{p,sel}$ = 60 ns. τ was set to 200 ns at 100 K, while the interpulse delay T was incremented (T_0 = 100 or 200 ns). Three-pulse ESEEM data were detected using π/2 – τ – π/2 – T – π/2 – τ – echo with a 4-step phase-cycle at 50 K. The π/2 pulse had a length of 16 ns. The constant delay τ was set to a proton blind spot at τ = 344 ns. The interpulse delay T had a starting value of 80 ns and was incremented in steps of 8 ns. Relaxation and three pulse ESEEM experiments were performed at the maximum of the Gd(III) spectrum.

6.2 Echo-detected EPR spectra

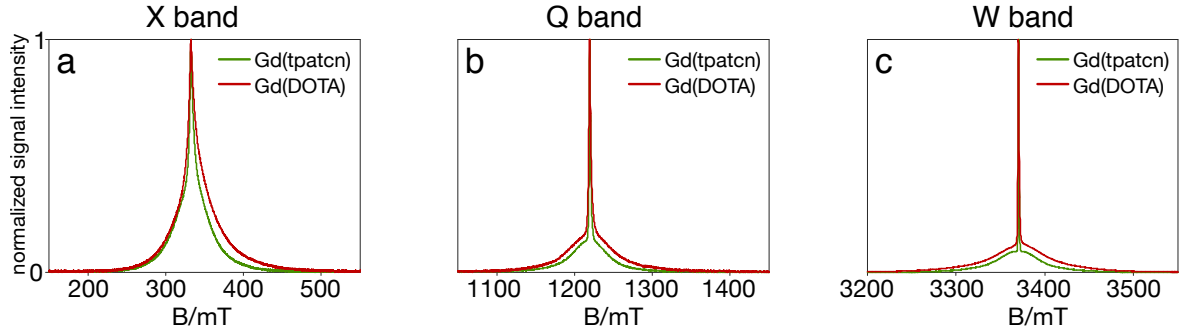

Figure SI-6: Echo-detected EPR spectra acquired for 25 µM frozen solutions of **(1)** and **(2)** at 100K in glycerol-d_8:D_2O:H_2O (60:30:10 v%) at X-, Q- and W-band (respective detection frequency of 9.5 GHz, 35 GHz, 94 GHz).

Figure SI-6 shows echo-detected EPR spectra of the 25 µM frozen solutions of **(1)** and **(2)** at 100K at three different detection fields/frequencies. At X band (**Figure SI SI-6(a)**) the ZFS parameter D is only about an order of magnitude smaller than the electron Zeeman splitting, and thus the central transition in the Gd(III) EPR spectrum is broad and merges with the sub-spectra of other transitions. At higher detection fields/frequencies the width of the sub-spectrum of the central transition reduces, following the change of the value D^2/ω_{0S} (i.e. inverse proportional to the resonance field). At the same time, the widths of sub-spectra for other Gd(III) EPR transitions remain approximately the same, which leads to a better resolved central peak (m_s=+1/2↔m_s=-1/2 transition) in the Gd(III) EPR spectrum. Note that the EPR spectrum of [Gd(tpatcn)] is narrower than the EPR spectrum of $[Gd(dota)(H_2O)]^-$ at each detection frequency, which is a strong indication of the difference in the ZFS distributions, with [Gd(tpatcn)] showing weaker ZFS.

Further, quantitative ZFS parameters can be extracted from the EPR lines [12-15].
It is important to note that already at concentrations of 10 mM, significant broadening of the central line occurs due to electron-electron couplings (see **Figure SI SI-8**). Thus, the ZFS parameters were extracted at low concentrations, where dipolar broadening is minimized.

At 10 K, following the procedure described previously in reference [16], on a series of Gd^{3+} complexes in deuterated water:glycerol mixtures, the ZFS parameter D of $[Gd(dota)(H_2O)]^-$ has a mean value of D = 733±64 MHz with a Gaussian distribution with standard deviation σ_D = 270±134 MHz. For [Gd(tpatcn)] we obtain, D = 525±30 MHz and σ_D = 174±72 MHz. The E parameter follows the distribution $P(E/D) = (E/D) - 2*(E/D)^2$ [13]. In both cases, the determined values are slightly larger than previously determined in deuterated water:glycerol mixtures, which may be related to the influence of

the solvent on the ligand arrangement. Nevertheless, the error bands in the two studies of the same complex overlap. At 100 K, transition-dependent relaxation significantly influences the EPR lineshape (see **Figure SI-7**) and the apparent ZFS values extracted from such lineshapes are reduced (D = 599 ± 94 MHz and σ_D = 330 ± 214 MHz for [Gd(dota)(H_2O)]$^-$ and D = 410 ± 25 MHz and σ_D = 106 ± 62 MHz for [Gd(tpatcn)]).

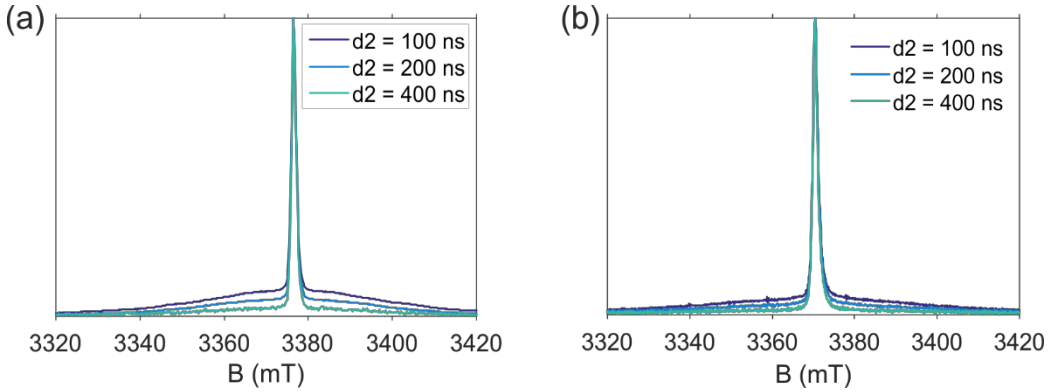

Figure SI-7: EDEPR spectra of (a) [Gd(tpatcn)] and (b) [Gd(dota)(H_2O)]$^-$ at 100 K, W band and 25 µM concentration. The outer transitions already significantly decay if the interpulse delay τ is increased from 100 to 200 to 400 ns.

This finding may be related to a more restricted motion around the Gd(III) centre at 10 K or to larger strain in the solvent glass at lower temperature. However, the fast decay of the outer EPR transitions makes extraction of the ZFS parameters at 100 K problematic and careful inspection of the fits (see **Figure SI-12**, **SI-13** and **SI-14**) shows that the width of the central line is underestimated, indicating that the extracted ZFS parameters are too small.

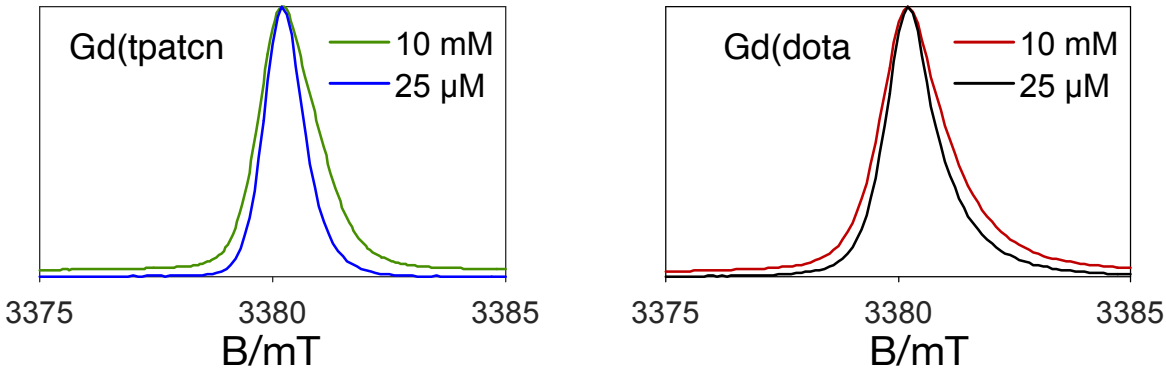

Figure SI-8: Echo-detected magnetic field sweep for the compounds [Gd(tpatcn)] and [Gd(dota)(H_2O)]$^-$ at 100 K, W band and 10 mM or 25µM concentration in glycerol-d_8:D_2O:H_2O (60:30:10 v%).

6.3 T_{1e} and T_{2e} measurements

The T_{1e} and T_{2e} values are reported in **Table 1** in the main text. At 25 µM the average distance between Gd complexes is about 50 nm (e.g. twice the Wigner-Seitz radius $R_{ws}=2(3/4\pi CN_A)^{1/3}$) with C the concentration and N_A the Avogadro number [17]. At 10 mM the average distance is reduced to around 7 nm. While a slightly larger (about 25%) saturation factor is present at 25 µM for [Gd(tpatcn)], no significant difference between the saturation factors of the two complexes emerges at 10 mM. At higher concentrations, and shorter distances, mutual spin-spin interactions introduce a strong additional relaxation pathway resulting in similar T_{1e} and T_{2e} (data in **Figure SI-9**).

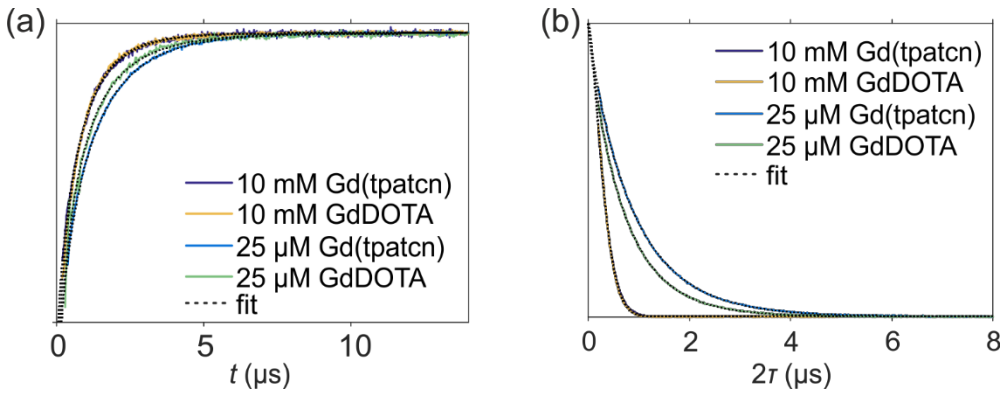

Figure SI-9: (a) Inversion Recovery and (b) Hahn echo decay for the compounds **(1)** and **(2)** at 100 K, W band and 25 μM or 10 mM concentrations in glycerol-d_8:D_2O:H_2O (60:30:10 v%). Black dashed lines show the corresponding fits.

7 EPR data analysis

7.1 Relaxation measurements

Relaxation data were analyzed using home-written MATLAB (The MathWorks Inc., Natick, MA, USA) scripts. Inversion recovery traces were inverted and subsequently fitted by stretched exponential functions of the form $c \cdot \exp(-(t/T_1)^{\xi})$ using a nonlinear least-square fitting criterion. Longitudinal relaxation times T_1 were then extracted from the fit parameter. Errors are extracted from the 95% confidence intervals of the fit. Hahn echo decay traces were processed by removing a constant offset. The data were then fitted by stretched exponential functions of the form $c \cdot \exp(-(t/T_m)^{\xi})$ using a nonlinear least-square fitting criterion. Errors are extracted from the 95% confidence intervals of the fit. T_m, T_1 and ξ parameters are given in **Table SI-4** below. Due to the fast decays an additional uncertainty was taken into account by combing relaxation traces with initial time increment of 100 and 200 ns.

	10 mM	**25 µM**	**10 mM**	**25 µM**
	T_m/ µs	T_m/ µs	T_1/ µs	T_1/ µs
[Gd (tpatcn)]	0.32 ± 0.06	0.84 ± 0.08	0.7 ± 0.1	0.9 ± 0.1
[Gd(dota)(H_2O)]$^-$	0.32 ± 0.05	0.71 ± 0.06	0.7 ± 0.1	0.8 ± 0.1
	ξT_m	ξT_m	ξT_1	ξT_1
[Gd (tpatcn)]	1.72 ± 0.23	0.92 ± 0.03	0.86 ± 0.04	0.83 ± 0.11
[Gd(dota)(H_2O)]$^-$	1.47 ± 0.15	0.93 ± 0.09	0.83 ± 0.12	0.75 ± 0.06

Table SI-4: Extracted T_m, T_1 and stretched exponential fitting parameters ξ for both complexes at 10 mM (brown) and 25 µM (gray) in W-band at 100 K.

7.2 Three-pulse ESEEM

The three-pulse ESEEM data were analyzed with a home-written MATLAB program provided in reference [18]. The background decay was subtracted by division of a 3rd-order polynomial fit to the primary data. The frequency domain spectrum was obtained after apodization with a Hamming window, zero filling, and finally computing the magnitude spectrum after Fourier transform.
The measurement-compensated water accessibility parameter was calculated according to reference [18]:

$$\Pi(D_2O) = \frac{2k_D}{[1-\cos(2\pi\nu_D\tau)]} \cdot \left(\frac{\nu_D}{2\ \mathrm{MHz}}\right)^2 \quad \text{(S 6)}$$

where τ is the interpulse delay. Normalization to a standard value of 2 MHz allows for a direct comparison with reference [19]. The deuterium modulation depth k_D was obtained by a least square fit of a damped harmonic oscillation

$$D(t) = k_D \cos(2\pi\nu_D T + \varphi) e^{\frac{-T^2}{\tau_0^2}} \quad \text{(S 7)}$$

with deuterium frequency ν_D, damping constant τ_0, and phase φ. The corresponding fits are shown in **Figure SI- SI-10**.

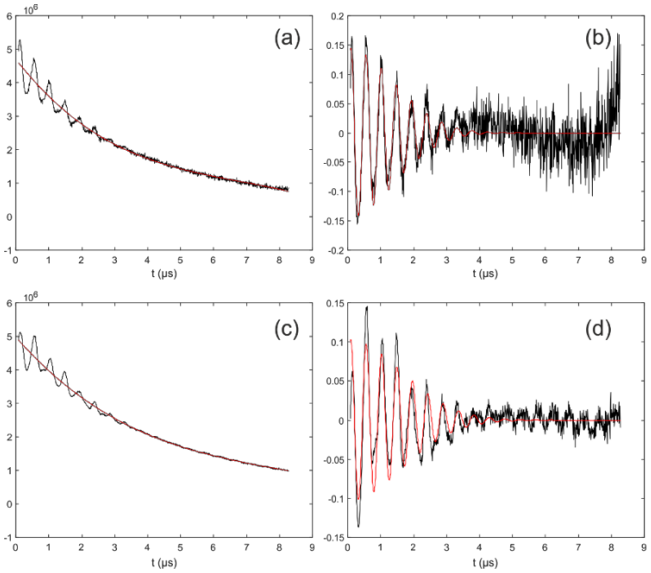

Figure SI-10: Three-pulse ESEEM experiment of $[Gd(dota)(H_2O)]^-$ (a, b) and [Gd(tpatcn)] (c, d) at 50 K in X-band. (a, c) primary data (black lines) and corresponding background fit (red lines); (b, d) background-corrected primary data with corresponding fit (red lines) according to Equation (S 9).

7.3 ZFS parameters determination

ZFS parameters were extracted according to reference [16] using Model 3. The EPR spectra of the Gd(III) complexes were simulated in MATLAB with home written scripts based on the EasySpin toolbox [20]. Absorption powder spectra were computed using full matrix diagonalization with the EasySpin function *pepper*. Orientation averaging was performed in 3-degree increments and a 10-fold interpolation of the orientation grid. The magnetic field range for simulation well covered the experimental one. The number of field points was set to 8000 to reach sufficient convergence. The spin system structure was defined as a single spin S=7/2 with an isotropic g-value of 1.992. The ZFS parameter D was sampled by a weighted bimodal Gaussian distribution with mean value D and width σ_D. For sampling the ZFS parameter E a probability distribution $P(E/D) = (E/D) - 2\ (E/D)^2$ was assumed [13]. For $[Gd(dota)(H_2O)]^-$ an asymmetry of $P(+D)/P(-D) = 0.3$ was assumed according to [16]. The [Gd(tpatcn)] complex, which is the same as the NO_3Pic complex in reference [16], has a very symmetric spectrum and thus the bimodal Gaussian was weighted equally. Additional line broadening parameters were set to zero in the simulations. The individual transitions of the S=7/2 spin system were summed with a weighting factor according to their effective flip angles.
ZFS parameters were extracted by comparing the simulated lineshapes from a ZFS library [16] to the experimental data according to a RMSD criterion (see **Figure SI-11**).

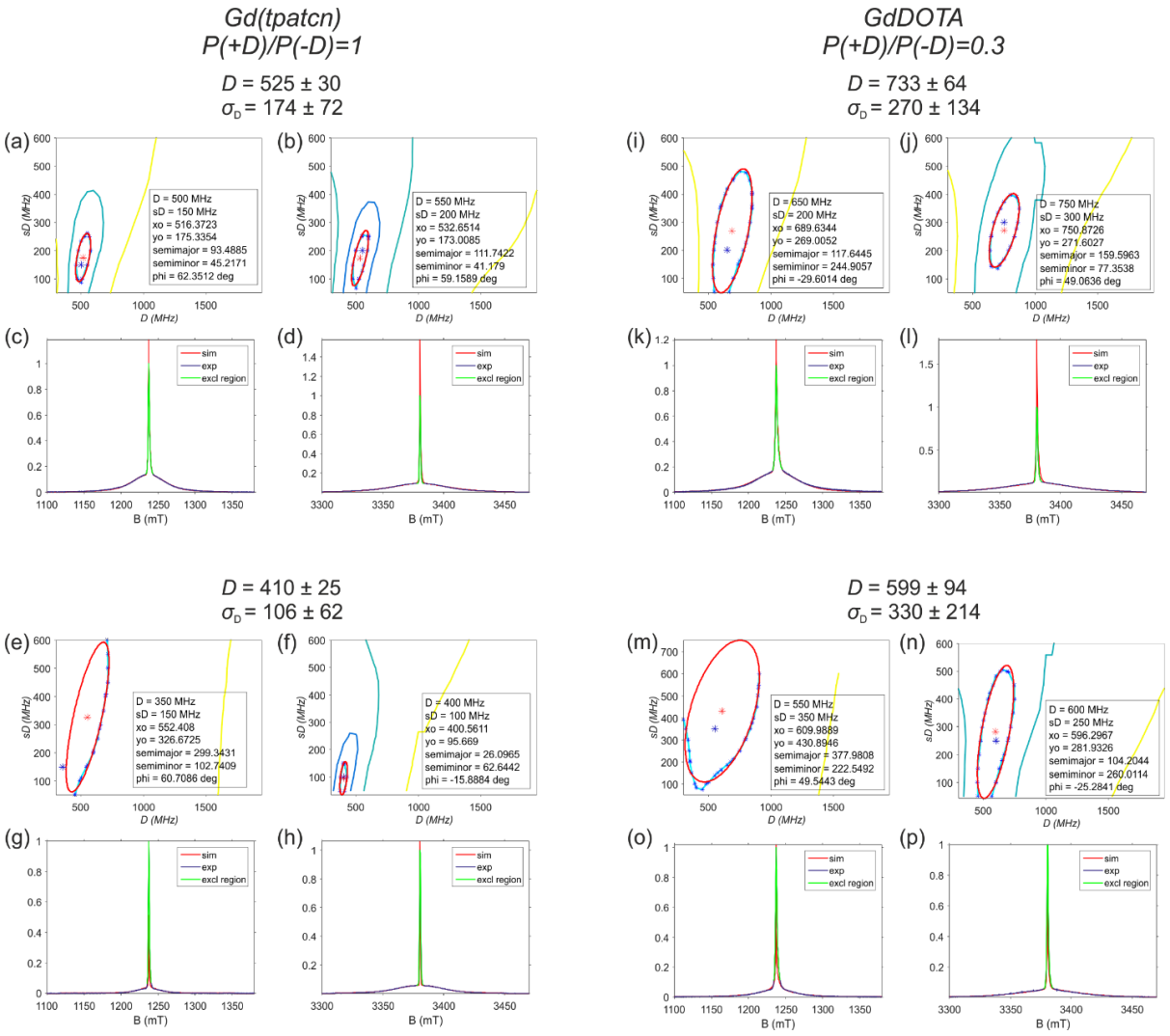

Figure SI-11: Extraction of ZFS parameters from the EPR lineshape. (a - h) 25 µM [Gd(tpatcn)] and (i - p) 25 µM [Gd(dota)(H_2O)]$^-$ with a weighted average of the extracted for D and σ_D and their associated errors from fitting Q and W band data. (a - d, i - l) 10 K; (e-h, m-p) 100 K. Please note, that the ZFS parameters at 100 K are possibly underestimated due to anisotropic relaxation. (a, b, i, j, e, f, m, n) Contours of constant RMSD as a function of D and σ_D parameter values. Each contour line represents a doubling of the minimum RMSD value, which is marked by the blue asterisk. An ellipse (red lines) was fitted to the first contour line. The center of the ellipse is marked by a red asterisk from which the best values of D and σ_D are estimated. The errors on the D and σ_D parameters are given by the lengths of the semi-minor and semi-major axes of the fitted ellipse. From details on the analysis routine (see reference **[7]**). (c, d, g, h, k, l, o, p) EPR spectra (purple line) and lowest RSMD simulation from the ZFS library (red line). The central region excluded from the RMSD calculation is marked in green. Simulated spectra were scaled by a least-squared criterion to the experimental data excluding the central region.

The ZFS library was created based on a 20000 points large Monte-Carlo ensemble for the D distribution and a measurement temperature of 10 K. The central region was excluded from the RMSD calculation, as it is most sensitive to additional line broadening contributions, different from ZFS, which were neglected in the lineshape calculations. Excluding the height of the central transition, the lineshape simulations at 100 K reveal only minor differences to lineshape simulations at 10 K (see **Figure SI-12**). Note again that relaxation effects, shown e.g. in the **Figure SI-7**, were not included in the EPR simulations.

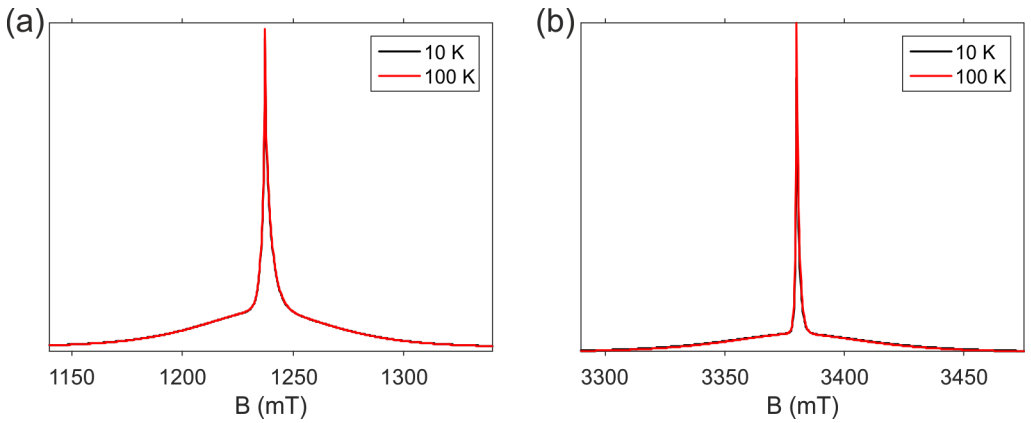

Figure SI-12: Comparison of simulated lineshapes at 10 K and 100 K with D = 733 MHz and σ_D = 270 MHz. (a) Q band, (b) W band. This figure indicates no strong difference in the EPR lineshape due to the changes in thermal polarization at 10K and 100K.

Thus, the same library was used to extract the ZFS parameters of the data measured at 100 K. The final fits for 10 and 100 K data were simulated using a 40 000 point large Monte-Carlo ensemble and the respective measurement temperature (**Figure SI-13** and **SI-14**).

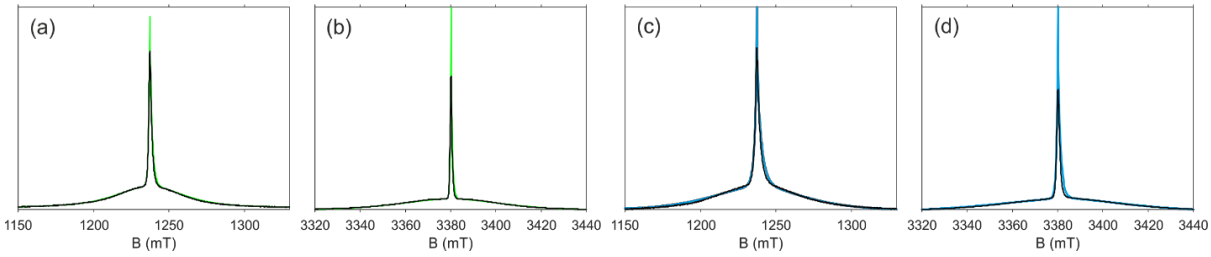

Figure SI-13: Comparison between experimental (black lines) and best-fit simulated lineshape (colored lines) at 10 K. (a, c) Q band, (b, d) W band. (a, b) Gd(tpatcn): D = 525 MHz and σ_D = 174 MHz. (c, d) Gd-DOTA: D = 733 MHz and σ_D = 270 MHz.

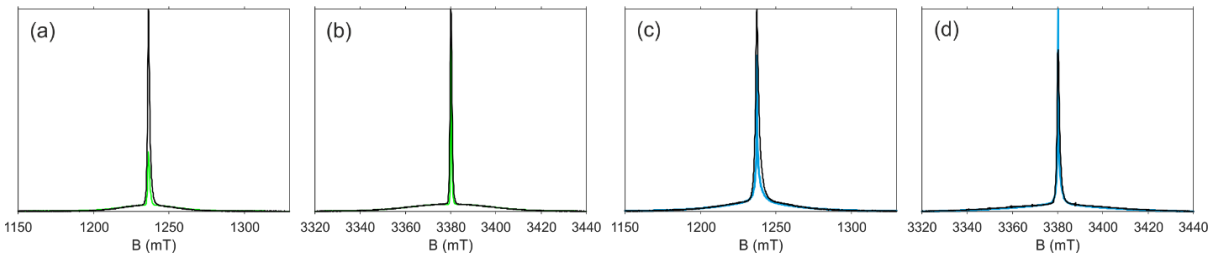

Figure SI-14: Comparison between experimental (black lines) and best-fit simulated lineshape (colored lines) at 100 K. (a, c) Q band, (b, d) W band. (a, b) Gd(tpatcn): D = 410 MHz and σ_D = 106 MHz. (c, d) Gd-DOTA: D = 599 MHz and σ_D = 330 MHz.

Extensive details on the data analysis, the model used and the numerical simulations can be found in reference [16].

7.4 ZFS library and simulation scripts

The ZFS library and scripts for the fitting routine can be extracted from http://www.epr.ethz.ch/software.

8 SI References

1. Nocton, G.; Nonat, A.; Gateau, C.; Mazzanti, M., Water Stability and Luminescence of Lanthanide Complexes of Tripodal Ligands Derived from 1,4,7-Triazacyclononane: Pyridinecarboxamide versus Pyridinecarboxylate Donors. *Helv Chim Acta* **2009,** *92* (11), 2257-2273.
2. Gateau, C.; Mazzanti, M.; Pecaut, J.; Dunand, F. A.; Helm, L., Solid-state and solution properties of the lanthanide complexes of a new tripodal ligand derived from 1,4,7-triazacyclononane. *Dalton T* **2003,** (12), 2428-2433.
3. Kubicki, D. J.; Rossini, A. J.; Purea, A.; Zagdoun, A.; Ouari, O.; Tordo, P.; Engelke, F.; Lesage, A.; Emsley, L., Amplifying Dynamic Nuclear Polarization of Frozen Solutions by Incorporating Dielectric Particles. *J Am Chem Soc* **2014,** *136* (44), 15711-15718.
4. Kaushik, M.; Bahrenberg, T.; Can, T. V.; Caporini, M. A.; Silvers, R.; Heiliger, J.; Smith, A. A.; Schwalbe, H.; Griffin, R. G.; Corzilius, B., Gd(III) and Mn(II) complexes for dynamic nuclear polarization: small molecular chelate polarizing agents and applications with site-directed spin labeling of proteins. *Phys Chem Chem Phys* **2016,** *18* (39), 27205-27218.
5. Mieville, P.; Ahuja, P.; Sarkar, R.; Jannin, S.; Vasos, P. R.; Gerber-Lemaire, S.; Mishkovsky, M.; Comment, A.; Gruetter, R.; Ouari, O.; Tordo, P.; Bodenhausen, G., Scavenging Free Radicals To Preserve Enhancement and Extend Relaxation Times in NMR using Dynamic Nuclear Polarization (vol 49, pg 6182, 2010). *Angew Chem Int Edit* **2010,** *49* (43), 7834-7834.
6. Smith, A. A.; Corzilius, B.; Barnes, A. B.; Maly, T.; Griffin, R. G., Solid effect dynamic nuclear polarization and polarization pathways. *J Chem Phys* **2012,** *136* (1).
7. Wenckebach, W. T., *Essentials of Dynamic Nuclear Polarisation*. Spindrift Publications: The Netherlands 2016.
8. Corzilius, B.; Smith, A. A.; Barnes, A. B.; Luchinat, C.; Bertini, I.; Griffin, R. G., High-Field Dynamic Nuclear Polarization with High-Spin Transition Metal Ions. *J Am Chem Soc* **2011,** *133* (15), 5648-5651.
9. Gromov, I.; Shane, J.; Forrer, J.; Rakhmatoullin, R.; Rozentzwaig, Y.; Schweiger, A., A Q-band pulse EPR/ENDOR spectrometer and the implementation of advanced one- and two-dimensional pulse EPR methodology. *J Magn Reson* **2001,** *149* (2), 196-203.
10. Polyhach, Y.; Bordignon, E.; Tschaggelar, R.; Gandra, S.; Godt, A.; Jeschke, G., High sensitivity and versatility of the DEER experiment on nitroxide radical pairs at Q-band frequencies. *Phys Chem Chem Phys* **2012,** *14* (30), 10762-10773.
11. Tschaggelar, R.; Kasumaj, B.; Santangelo, M. G.; Forrer, J.; Leger, P.; Dube, H.; Diederich, F.; Harmer, J.; Schuhmann, R.; Garcia-Rubio, I.; Jeschke, G., Cryogenic 35 GHz pulse ENDOR probehead accommodating large sample sizes: Performance and applications. *J Magn Reson* **2009,** *200* (1), 81-87.
12. Benmelouka, M.; Van Tol, J.; Borel, A.; Port, M.; Helm, L.; Brunel, L. C.; Merbach, A. E., A high-frequency EPR study of frozen solutions of Gd-III complexes: Straightforward determination of the zero-field splitting parameters and simulation of the NMRD profiles. *J Am Chem Soc* **2006,** *128* (24), 7807-7816.
13. Raitsimring, A. M.; Astashkin, A. V.; Poluektov, O. G.; Caravan, P., High-field pulsed EPR and ENDOR of Gd3+ complexes in glassy solutions. *Appl Magn Reson* **2005,** *28* (3-4), 281-295.
14. Buckmaster, H. A.; Shing, Y. H., Survey of Epr-Spectra of Gd3+ in Single-Crystals. *Phys Status Solidi A* **1972,** *12* (2), 325-+.
15. Raitsimring A.M., A. A. V., Caravan P., High-Frequency EPR and ENDOR Characterization of MRI Contrast Agents. In *High Resolution EPR.*, L. Berliner, G. H., Ed. Springer: New York, 2009; Vol. 28, pp 581-621.
16. Clayton, J. A.; Keller, K.; Qi, M.; Wegner, J.; Koch, V.; Hintz, H.; Godt, A.; Han, S.; Jeschke, G.; Sherwin, M. S.; Yulikov, M., Quantitative analysis of zero-field splitting parameter distributions in Gd(III) complexes. *Phys Chem Chem Phys* **2018,** *20* (15), 10470-10492.
17. Pinon, A. Spin Diffusion in Dynamic Nuclear Polarization Nuclear Magnetic Resonance. PhD Thesis n◦ 8519, Pag.1-136, Ecole Polytechnique Federale De Lausanne, Lausanne-Switzerland, July 31st 2018.

18. Volkov, A.; Dockter, C.; Bund, T.; Paulsen, H.; Jeschke, G., Pulsed EPR Determination of Water Accessibility to Spin-Labeled Amino Acid Residues in LHCIIb. *Biophys J* **2009,** *96* (3), 1124-1141.
19. Carmieli, R.; Papo, N.; Zimmermann, H.; Potapov, A.; Shai, Y.; Goldfarb, D., Utilizing ESEEM spectroscopy to locate the position of specific regions of membrane-active peptides within model membranes. *Biophys J* **2006,** *90* (2), 492-505.
20. Stoll, S.; Schweiger, A., EasySpin, a comprehensive software package for spectral simulation and analysis in EPR. *J Magn Reson* **2006,** *178* (1), 42-55.